

On the geometry of turbulent mixing

By EMMANUEL VILLERMAUX
AND CLAUDIA INNOCENTI

LEGI-CNRS, Institut de Mécanique de Grenoble BP 53X, 38041 Grenoble Cedex, France

(Received 6 April 1998 and in revised form 25 March 1999)

We investigate the temporal evolution of the geometrical distribution of a passive scalar injected continuously into the far field of a turbulent water jet at a scale d smaller than the local integral scale of the turbulence. The concentration field is studied quantitatively by a laser-induced-fluorescence technique on a plane cut containing the jet axis. Global features such as the scalar dispersion from the source, as well as the fine structure of the scalar field, are analysed. In particular, we define the volume occupied by the regions whose concentration is larger than a given concentration threshold (support of the scalar field) and the surface in which this volume is enclosed (boundary of the support). The volume and surface extents, and their respective fractal dimensions are measured as a function of time t , and the concentration threshold is normalized by the initial concentration C_s/C_0 for different injection sizes d . All of these quantities display a clear dependence on t , d and C_s , and their evolutions rescale with the variable $\xi = (ut/d)(C_s/C_0)$, the fractal dimension being, in addition, scale dependent. The surface-to-volume ratio and the fractal dimension of both the volume and the surface tend towards unity at large ξ , reflecting the sheet-like structure of the scalar at small scales. These findings suggest an original picture of the kinetics of turbulent mixing.

1. Introduction

It is of common experience that mixing, the process which aims at reaching uniformity of a set of two or more initially segregated constituents, induces complex, stretched and folded structures, interlacing the phases while they interpenetrate. Practical examples may range from the deformation of a drop of milk in a stirred cup of coffee to the large-scale patterns of contaminants in geophysical flows (see e.g. Ottino 1989 for a review).

The involved, multiscale geometry of the interface between the two streams being mixed is not only a spectacular facet of the process, but is sometimes at the core of the physical problem, such as for combustion of premixed, or unpremixed reactants. The total extent of the flame area dictates the propagation speed of the flame in the first case (Damköhler 1940), and the net combustion rate in the second (Hawthorne, Wendell & Hottel 1949; Villermaux 1995).

Notwithstanding the fact that mixing is, in the strict sense, a transient process, the attack on the problem of a passive scalar convected in a turbulent flow has focused on hypothetical 'stationary conditions'. This approach parallels the quasi-equilibrium picture of turbulence (Oboukhov 1949; Corrsin 1951) and in this limit it is assumed that the timescales of the stirring motions which distort the scalar field are all shorter, at least in a certain wavenumber range, than the global mixing time (i.e. the variance

of the scalar fluctuations is stationary), allowing the possibility of resorting to cascade arguments, and spectral analysis.

The dissipation scale of the scalar η_B in this frame is then estimated from a balance between a stretching time at small scales, independent of the scalar injection scale, and a diffusion time. It was shown by Batchelor (1959) and Batchelor, Howells & Townsend (1959) that depending on whether the Schmidt number ν/D is smaller or larger than unity, where D denotes the diffusivity of the scalar, the stretching time has to be estimated in the viscous range (for $Sc \gg 1$) leading to $\eta_B = \eta Sc^{-1/2}$ or in the inertial range (for $Sc \ll 1$), leading to $\eta_B = \eta Sc^{-3/4}$, η being the Kolmogorov scale, i.e. the dissipation scale of vorticity, whose diffusivity is ν .

In keeping with this approach where the absolute time has disappeared, several investigators have subsequently tried to describe not only the characteristic scales of the mixture, but its global geometry through a number indicative of the hierarchy of motions giving birth to the complexity of the scalar field, namely fractal dimensions (Mandelbrot 1975). The fractal nature of interfaces separating a turbulent from a non-turbulent medium (Sreenivasan, Ramshankar & Meneveau 1989; Meneveau & Sreenivasan 1990; Prasad & Sreenivasan 1990), of iso-scalar contours in turbulent flows (Constantin, Procaccia & Sreenivasan 1991; Lane-Serff 1993; Flohr & Olivari 1994; Catrakis & Dimotakis 1996) or random flows (Ramshankar & Gollub 1991; Gluckman, Willaime & Gollub 1993; Cardoso *et al.* 1996) has been demonstrated either on two-dimensional sections, or on one-dimensional cuts through the scalar field (Miller & Dimotakis 1991; Sakai *et al.* 1995; Frederiksen, Dahm & Dowling 1996).

Though all of these studies agree that, at least on a certain range of scales and concentration levels, interfaces and iso-concentration contours are less smooth than a Euclidean surface (i.e. the dimensions of contours extracted from two-dimensional cuts are generally found to be larger than unity), the possible scale dependence, Reynolds number dependence (see Catrakis & Dimotakis 1996 and references therein), threshold height of the level set dependence (Prasad & Sreenivasan 1990; Miller & Dimotakis 1991; Lane-Serff 1993; Flohr & Olivari 1994; Sakai *et al.* 1995), scalar diffusivity dependence (Gluckman *et al.* 1993) and time dependence when the scalar is followed along its transient evolution (Ramshankar & Gollub 1991; Villermaux & Gagne 1994; Nicolleau 1996) of the usually defined dimension have never been considered on a general basis.

Transients and time dependences are explicitly taken into account in studies on dispersion addressing the problem of the radius growth rate of a tracer blob immersed in a prescribed displacement field. In addition to pure molecular diffusion on the still substrate, motions in flows usually enhance dispersion (Taylor 1921, 1953) and even alter the diffusion law, not only by a renormalization of the diffusion coefficient, but the structure of the law itself. Due to persistent ballistic motions, and ever larger jumps in turbulent flows, dispersion laws exhibit, in the absence of traps or slow recirculating motions, a rate of growth of the mean-squared radius of the blob which can be faster than linear in time (Richardson 1926). The presence of bypasses or dead-ends in complex geometries alters, in continuous flow systems (e.g. a river, a valley through which wind blows, an open chemical reactor), the residence time distribution of a tracer deposited at the inlet of the system. The novel features of this distribution are spikes at short times if a short circuit is present, and/or long tails caused by traps and slow motions in confined cavities as first described by Danckwerts (1953).

Dispersion may result solely from a spatial reorganization of the quantity to be mixed, with no interpenetration with the substrate at the molecular level. Mixing,

as opposed to stirring, actually means homogenization at the smallest, i.e. diffusive, scales. The mixing time (for instance in a tank stirred with an impeller familiar in the chemical industry) is known to be solely determined by the large-scale features of the flow (integral scale, root-mean-square velocity, see e.g. Nagata 1975), regardless of the intimate structure of the turbulence, provided the Reynolds number is high enough (typically larger than 10^4), in a wide variety of flows. The order of magnitude of this critical Reynolds number for the onset of the ‘mixing transition’ has been documented in shear layer experiments (Breidenthal 1981; Koochesfahani & Dimotakis 1986), as well as its sensitivity to the initial contacting conditions between the streams (Huang & Ho 1989; Kassaro & Mungal 1996). These studies emphasize the role of the persistent large-scale motions in the interpenetration between the phases. A more recent study has shown that the mixing time is proportional to the injection scale of the scalar when the latter is smaller than the integral scale of the flow (Villermaux, Innocenti & Duplat 1998).

Watching the dynamics of material ‘coloured bands’ (O. Reynolds) in a flow may, following the early suggestions of Reynolds (1894) and also Welander (1955) reveal the nature of the underlying motion. We suggest here that the study of the birth and kinetics of the complexity of an initially regular scalar field in a purposely designed transient configuration is a key route for understanding the mechanisms of turbulent mixing.

2. Experimental setup and procedures

2.1. Flow configuration

The present experiment consists in following the sequence of events which contribute to the incorporation and mixing of a scalar stream released in a sustained turbulent medium.

To obtain information about the kinetics of the incorporation process, we purposely decouple the development of the turbulent velocity field from the process of mixing. We use a water jet discharging into a large tank filled with water at rest as a turbulence generator and we inject the scalar continuously through a tube, in the direction of the mean flow and at the same velocity (figure 1). The exit velocity of the injection tube is maintained constant and equal to the mean velocity of the main jet carrying the turbulence at the injection point so that the tube behaves neither as a source nor as a sink of momentum, in the mean. The diameter of the tubes d can be varied but remains smaller than the turbulence integral scale L so that the mixing distance from the injection point (respectively the mixing time) is smaller than the integral scale (respectively the integral turnover time) for the turbulence to remain fairly stationary compared to the natural evolution of the mixing (see Villermaux *et al.* 1998 for a discussion of the mixing times). We use three tubes such that $d/L = 0.05, 0.1$ and 0.16 .

The injection tube is placed 30 diameters downstream of the turbulence generator jet exit. The local integral scale ($L = 6$ cm) was measured and found to be consistent with the relation proposed by Antonia, Satyaprakash & Hussain (1980). The r.m.s. velocity u' is about 25% of the mean velocity u , giving a turbulent Reynolds number $Re = u'L/\nu = 6000$ for $u = 0.4$ m s⁻¹, and 12 000 for $u = 0.8$ m s⁻¹. The distance x is computed from the injection tube exit, and we relate space to time via $x = ut$.

The presence of the injection tube was checked not to perturb a region of more than 2 diameters d downstream of the injection point. Both the velocity power spectrum

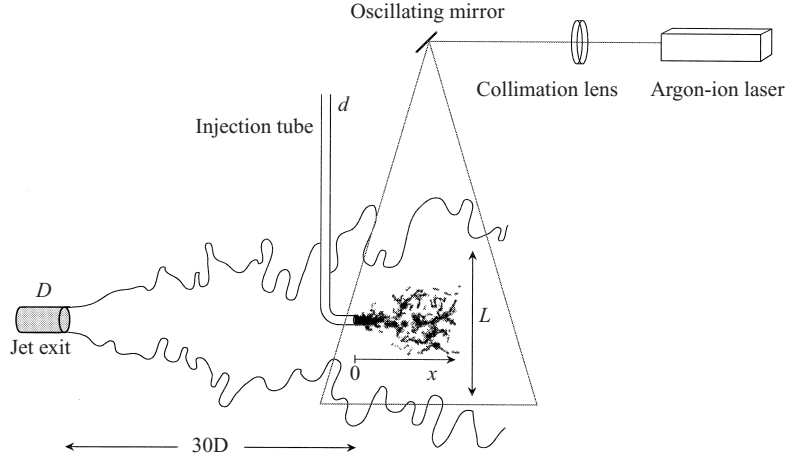


FIGURE 1. Sketch of the experiment. The scalar is injected by a small tube of diameter d on the axis and 30 diameters D downstream of the turbulence generator jet exit. $D = 2.7$ cm. The scalar injection scale ($d/L = 0.05, 0.1, 0.16$) lies in the inertial range of the turbulent flow field, i.e. $\eta = LRe^{-3/4} < d < L$ with $L = 6$ cm. $Re = u'L/\nu \approx 10^4$.

($E_u(k) \sim k^{-5/3}$) and the PDF of the longitudinal velocity increments for a separation distance of d i.e. $\delta u_x(d) = \langle u_x(x+d) - u_x(x) \rangle$ were identical to their free-stream analogues (with the tube removed) for $x/d \gtrsim 2$.

2.2. Visualization methods

The images of the scalar field were obtained by a standard laser-induced-fluorescence technique. We use disodium fluorescein as a laser-fluorescent dye, the Schmidt number being about $Sc = 2000$. A thin laser sheet is produced by spanning a 5.4 W Argon-ion laser beam, collimated by a long-focal-length lens ($f = 2$ m) with a mirror oscillating at 4 kHz. This provides a uniformly illuminated region in the visualization window; the thickness of the sheet is of the order of $300 \mu\text{m}$. The images are acquired by a SONY D7CE video camera with a Paillard 75 mm $f/2.8$ lens at a rate of 25 images per s and exposure time of $1/1000$ s. They were either directly digitized by a NEOTECH 8 bits A/D converter and written to the computer disk, or stored on a S-VHS magnetoscope, and further digitized and processed. The images are initially digitized on 768×512 pixels and were shrunk to 384×256 pixels before processing. The pixel size on a final image corresponds to a real dimension of $125 \mu\text{m}$, a distance slightly above the Kolmogorov scale ($\eta \approx 100 \mu\text{m}$ at $Re = 6000$), itself 44 times larger than the Batchelor dissipation scale $\eta_B = \eta Sc^{-1/2}$. The dissipation scale relevant to that configuration (Villermaux *et al.* 1998) is $s_D = d(Re_d Sc)^{-1/2}$, with $Re_d = ud/\nu$ the injection tube Reynolds number. It is in that case of the same order as the Batchelor scale.

Each pixel thus receives a fluorescence signal integrated on a $125 \times 125 \times 300 \mu\text{m}^3$ volume. The calibration of the background-subtracted images is linear up to the injection concentration $C_0 = 5 \times 10^{-7} \text{ mol l}^{-1}$, corresponding to a grey level of 155 . The r.m.s. noise of the images is less than 1% of the injection concentration. A lower injection concentration level resulted in negligible laser attenuation across the visualization window.

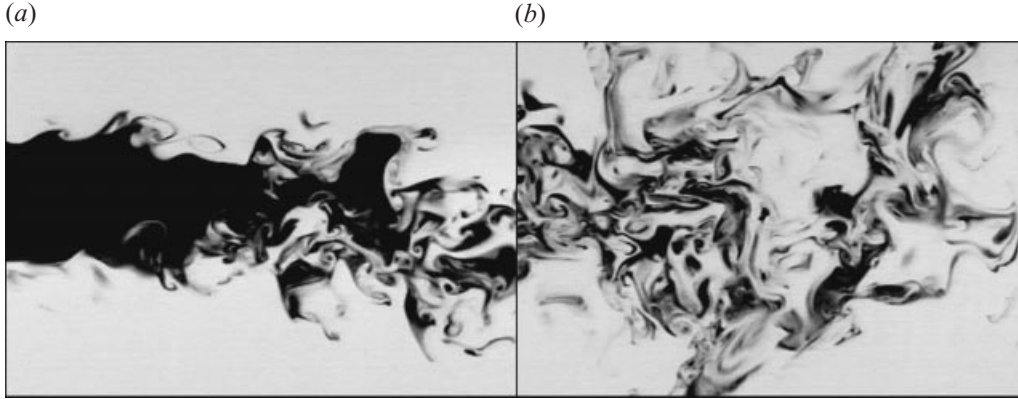


FIGURE 2. Instantaneous planar cuts through the scalar field downstream of the injection point; $d = 1$ cm, $u = 0.4$ m s⁻¹: (a) the region just downstream of the injection tube $0 < x/d < 4$; (b) farther downstream $4 < x/d < 8$.

3. Global quantities

The plume emerging from the source meanders in the radial direction while being progressively converted into disjointed sheets which are diluted in the surrounding turbulent medium (figures 2 and 6). The centre of mass of each scalar packet released from the source (whose size is of the order of d) is translated as a whole by large-scale motions (of the order of L) of the underlying turbulence.

We first depict the mean width of the plume downstream of the injection point, independently of the concentration level it carries. We thereby characterize the dispersion of the support of the scalar. We define the probability of presence of the scalar, $P_p(x, y)$, at each point (x, y) of each image, as

$$P_p(x, y) = \frac{1}{N} \sum_{i=1}^N p_i(x, y), \quad (1)$$

$$p_i(x, y) = 1 \quad \text{if } C_i(x, y) > C_d,$$

$$p_i(x, y) = 0 \quad \text{if } C_i(x, y) \leq C_d,$$

where $N = 500$ is the number of averaged images, $C_i(x, y)$ is concentration (grey level) of the i th image at point (x, y) and $C_d = 0.16C_0$ is the lowest concentration level which can be distinguished from the image background (detection threshold). The radial dispersion in the y -coordinate $\sigma(x)$ of the scalar plume support is the standard deviation of the radial distribution $P_p(x, y)$ at different downstream locations x :

$$\sigma(x) = \left(\int (y - \bar{y})^2 P_p(x, y) dy \right)^{1/2}, \quad (2)$$

and we have checked that $\bar{y} = \int y P_p(x, y) dy \approx 0$, i.e. that the distribution is centred on the axis of injection.

Figure 3(a) shows the resulting field of probability of presence for $d = 0.3$ cm, and figure 3(b) the radial dispersion $\sigma(t)$ as a function of time (remember that $t = x/u$) for the three different injection diameters d . Searching for the radial location of the centre of mass $y_{c_i}(x)$ of the instantaneous probability-of-presence distribution $p_i(x, y)$ on each image and on each slice of the image in the x -direction, we compute the standard

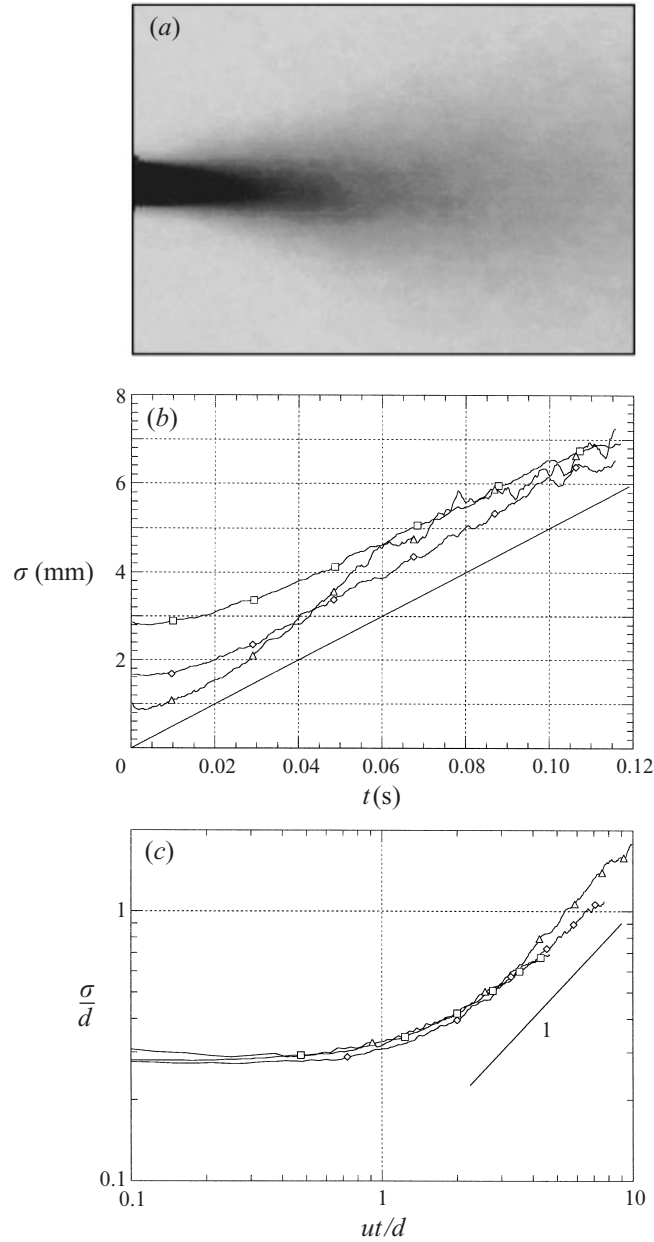


FIGURE 3. (a) Field of probability of presence of scalar $P_p(x, y)$ defined by equation (1) for $d = 0.3$ cm. (b) Standard deviation σ (equation (2)) of the radial distribution $P_p(x, y)$ with the distance x converted to time t by $x = ut$. \square , $d = 1$ cm; \diamond , $d = 0.6$ cm; \triangle , $d = 0.3$ cm. (c) Same as in (b) with the coordinate transformation of equation (3).

deviation of the centre of mass $\sigma_c(x) = \left(\frac{1}{N} \sum_{i=1}^N [y_{ci}(x) - \bar{y}_c(x)]^2 \right)^{1/2}$, where $\bar{y}_c(x) \approx 0$. We have checked that $\sigma_c(x) \approx \sigma(x)$. The dispersion $\sigma(t)$ is essentially dominated by the meandering motion of the plume whose transverse size remains of the order of d . This meandering motion is a consequence of the large-scale displacements caused

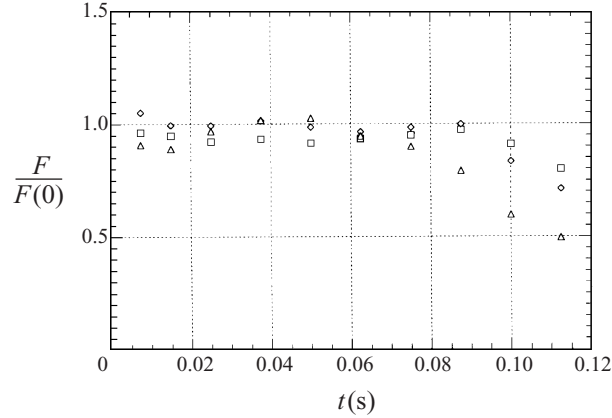


FIGURE 4. Net scalar flux $F(x)$ (equation (4)) through cross-sections downstream of the source ($t = x/u$). \square , $d = 1$ cm; \diamond , $d = 0.6$ cm; \triangle , $d = 0.3$ cm.

by the turbulence before the plume has been divided into disjointed sheets (see e.g. Stapountzis *et al.* 1986).

The role of the turbulent large-scale motions in the dispersion of the plume at these early stages is further confirmed by the fact that $\sigma(t)$ has, for $t > d/u$, a linear dependence on time t , with a slope, independent of d , of the order of half the r.m.s. turbulence velocity $\sigma(t) \approx \frac{1}{2}u't$ (figures 3b, 3c). Consequently, the $\sigma(t)$ -dependences all collapse on a single curve when rescaled according to the transformations (figure 3c)

$$\sigma \rightarrow \frac{\sigma}{d} \quad \text{and} \quad x \rightarrow \frac{x}{d}, \quad \text{that is} \quad t \rightarrow \frac{ut}{d}. \quad (3)$$

The conservation of the net scalar flux $F(x)$ through all cross-sections downstream of the source is written in axisymmetric coordinates as

$$F(x) = 2\pi u \int \bar{C}(x, y)y \, dy = F(0) = C_0\pi(d/2)^2u, \quad (4)$$

where we assume a constant velocity equal to u in the dispersion region, an approximation justified by the fact that $\sigma(x)/L \ll 1$. The mean concentration field $\bar{C}(x, y)$ is

$$\bar{C}(x, y) = \frac{1}{N} \sum_{i=1}^N C_i(x, y), \quad (5)$$

and it can be seen on figure 4 that the net flux is actually roughly conserved for all times. The slight decrease of $F(x)$ observed for $d/L = 0.1$ and $d/L = 0.16$ is due to the fact that for the largest values of d , the large radial excursions of the plume eventually exit the visualization window. The decrease of $F(x)$ for the smaller tube ($d/L = 0.05$) is due to the fact that, at large distances from the injection point, an appreciable fraction of scalar sheets have a concentration level below the detection threshold C_d and do not contribute to the integration (5). This 'loss of mass' is a manifestation of the fine-scale mixing process discussed in the two next sections.

The mean concentrations on the centreline $\bar{C}(x, 0)$ for the different injection diameters d rescale, again, in the $x/d = ut/d$ coordinates and follow a power law decrease

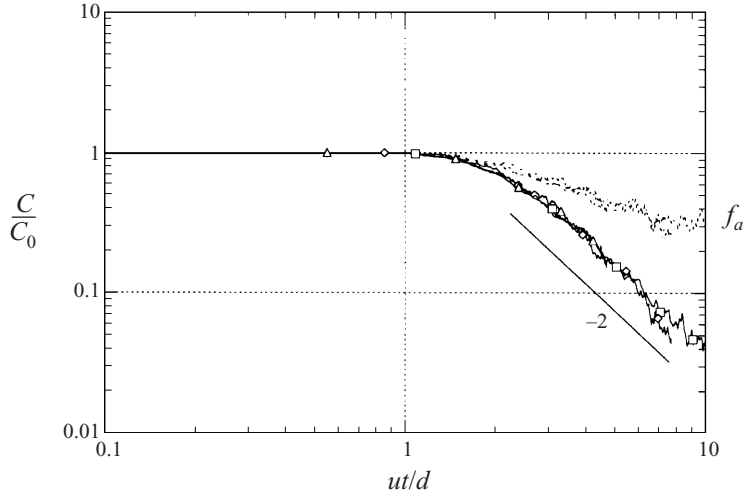


FIGURE 5. Continuous lines: mean concentration on the axis $\overline{C}(ut/d, 0)/C_0$ for the three diameters d . Dotted lines: ratio $f_a(t) = \overline{C}(ut/d, 0)/P_p(t, 0)$.

for $x/d \gtrsim 2$ (figure 5)

$$\frac{\overline{C}(ut/d, 0)}{C_0} \sim \left(\frac{ut}{d}\right)^{-2}. \quad (6)$$

This is an immediate consequence of the mass conservation constraint (4) together with the linear increase of the dispersion width σ (as shown on figure 3; the standard deviation computed from the concentration profile is parallel to σ). The exponent -2 is peculiar to the axisymmetric injection geometry. The decay law downstream of a line source (instead of a point source) would be characterized by an exponent -1 , as observed for instance in Stapountzis *et al.* 1986 (see also Csanady 1973; Tong & Warhaft 1995).

The mean concentration decay (6) is strictly related to the dispersion properties of the flow, themselves directly related to the meandering motion of the plume. Also included in figure 5 is the ratio of the mean concentration $\overline{C}(t, 0)$ to the probability of presence $P_p(t, 0)$ on the axis, i.e. $f_a(t) = \overline{C}(t, 0)/P_p(t, 0)$. It is clear that the ratio $f_a(t)$, which reflects the concentration decrease due to the true mixing by molecular diffusion, decreases more slowly than $\overline{C}(t, 0)$. The evolution law of f_a is related to the evolution of the one-point concentration PDF, as discussed below and in Villermaux *et al.* (1998).

4. Fine structure of the scalar distribution

4.1. Volumes and surfaces

We concentrate now on the geometry of the small scales of the scalar field inside the plume whose global dispersion properties have been described in the previous section. Our aim here is to characterize how the volume occupied by the scalar and the surface of the interface which separates the volume from the clear surrounding medium and in which it is enclosed evolve in time. Since we only have access to a planar cut of the three-dimensional structures through the scalar plume, by ‘volume’

and ‘surface’ we actually mean ‘area’ and ‘contour length’ of the objects we visualize on a two-dimensional image.

Figures 2, 6 and 13 show snapshots of the plume and of its subsequent degeneration into disjointed sheets. As described in the previous section, the scalar is initially confined in a compact region whose front is further distorted into multiscale elongated structures. As the core of the plume is converted into thin sheets, the concentration distribution widens and the scalar elements with a concentration close to the injection concentration get less and less numerous.

We choose a given concentration threshold C_s to define the geometrical support of the scalar field, that is the largest region of space occupied by the scalar, as seen with a detection level C_s . This threshold level might be different (higher) from the detection threshold C_d we chose in the previous section to define the support of the scalar. It is clear, in particular far from the injection point when the plume has appreciably diluted into the clear water, that the geometry of the scalar distribution is threshold dependent, because of the blurring action of diffusion on the definition of the contours. One might thus expect that both the surface and volume of the scalar support will present a concentration threshold dependence and our aim is precisely to determine their sensitivity to the choice of C_s , in addition to their natural dependences on d , u and t .

The sequence of operations for measuring volumes and surfaces as a function of time for a given threshold C_s is the following: we divide an instantaneous image into n vertical rectangles (figure 6) of size $w \times 256$ pixels, where $w = \text{int}(384/n)$. For example we chose $n = 9$ and $w = 40$ pixels in figure 6, corresponding to a real width of about 5 mm. The x -coordinate of the centre of each rectangle is

$$x_{c_j} = w/2 + (j - 1)w, \quad j = 1, n, \quad (7)$$

and corresponds to a convection time from the source of $t_j = x_{c_j}/u \pm w/2u$. Then (see figure 6), we proceed as follows:

(i) We binarize the image with respect the chosen concentration threshold C_s for five different relative levels, i.e. $C_s/C_0 = 0.16, 0.25, 0.38, 0.51$ and 0.63 according to

$$C_i(x, y) = 1 \quad \text{if } C_i(x, y) > C_s, \quad (8a)$$

$$C_i(x, y) = 0 \quad \text{if } C_i(x, y) \leq C_s. \quad (8b)$$

(ii) We differentiate the image pixel by pixel to extract the contours of the objects obtained by the conditional procedure (i). We thereby obtain the surfaces of the objects.

(iii) We sum the images obtained by the procedures (i) and (ii), thereby obtaining the volume of the objects, the volume being defined here as the sum of the pixels within closed contours plus the pixels constituting the contour.

The number of pixels different from zero contained into the j th rectangle of the images at steps (ii) and (iii) are respectively the measure of the instantaneous surface and volume of the mixture at time t_j . The mean values of the volume and surface are obtained by averaging over $N = 100$ images.

We defined the volume of the scalar as the sum of the binarized image plus its contour (step iii) to account for the fact that the volume of the smallest and thinnest objects (such as lines or points) are ‘confused’ with their boundaries. Another choice could have been made, for instance excluding the surface from the definition of the volume, with not many consequences on the relative evolutions of the surface and

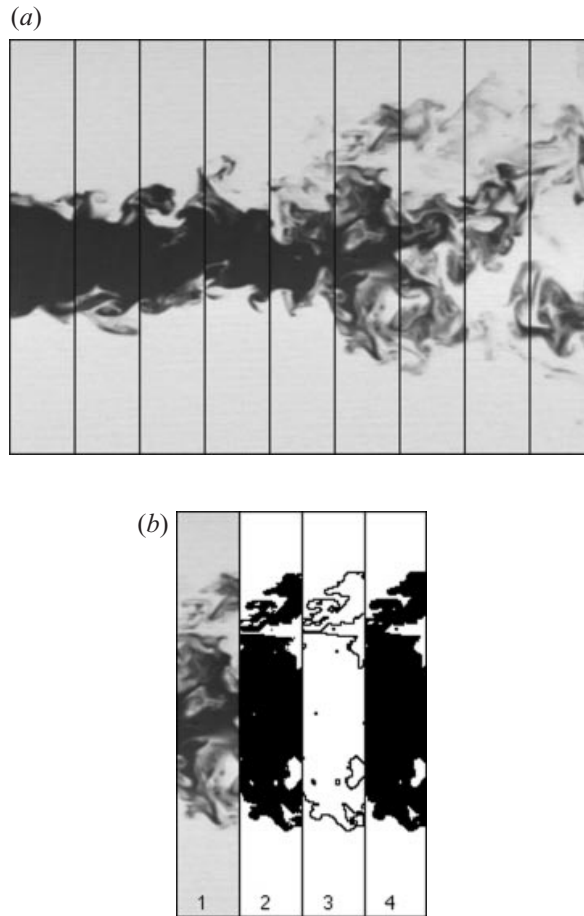


FIGURE 6. (a) Division of an image into nine equal rectangles. (b) Example of the procedure applied to the 6th rectangle of (a) to extract, after binarization (2), surface (3), and volume (4) of the object contained in (1).

of the volume as long as these are judged from discrete images built with finite-size elementary bricks, namely pixels.

For short times ($t \lesssim 2d/u$, see figure 7), the surface S increases fairly linearly with time t independently of C_s , but for $t > 2d/u$, the temporal evolution of S becomes strongly dependent on the threshold C_s . For the lowest values of C_s/C_0 , the surface continues to increase, although at a reduced rate, while for the highest values of C_s/C_0 , the surface evolution reaches a maximum, whose value increases as C_s/C_0 decreases, and then finally decreases as time goes on.

We will come back to this trend specifically in §5 but the general behaviour can at this point be explained heuristically in the following way: the stretching of the underlying turbulent motions tends to increase the extent of the plume front, producing the elongated structures observed, for instance on figures 2 and 6. This production activity is slowed down when molecular diffusion starts to become effective, smoothing the concentration distribution at the edge of the structures. At this point the surface extent becomes dependent on the concentration threshold C_s/C_0 . The subsequent decrease of the surface extent is a manifestation of the predominance

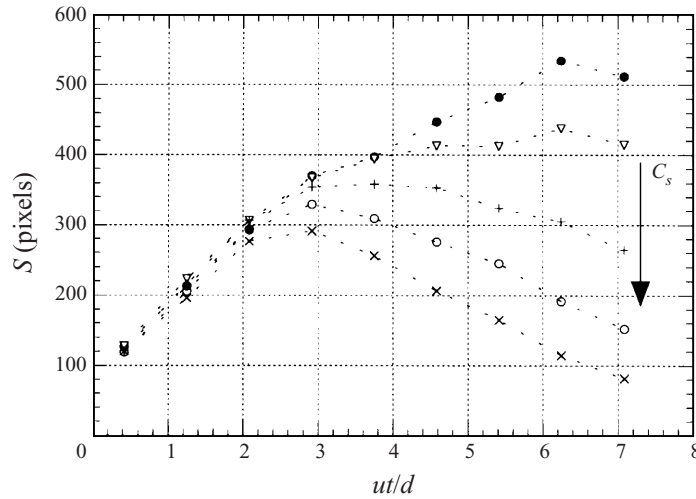


FIGURE 7. Surface of the plume as a function of ut/d for different values of the threshold height. In the direction of the arrow, $C_s/C_0 = 0.16, 0.25, 0.38, 0.51$ and 0.63 . $d = 0.6$ cm.

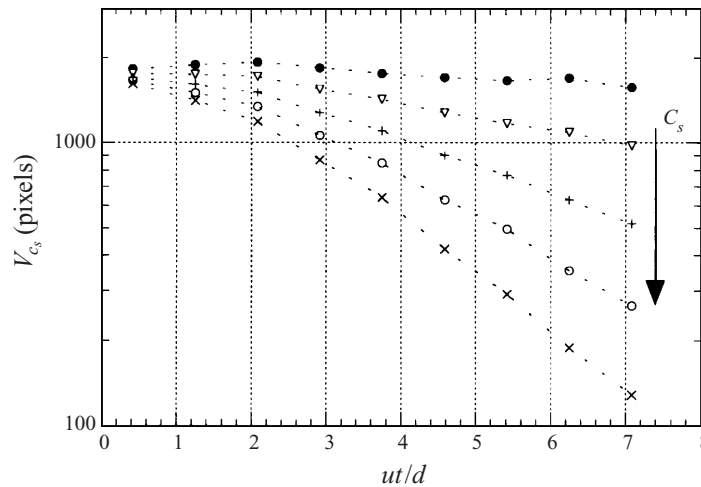


FIGURE 8. Volume of the plume as a function of ut/d for different values of the threshold height. In the direction of the arrow, $C_s/C_0 = 0.16, 0.25, 0.38, 0.51$ and 0.63 . $d = 0.6$ cm.

of the action of diffusion over the production mechanism. It is more pronounced, and happens earlier when the threshold is higher. Correspondingly, the volume V occupied by the scalar remains almost constant for thresholds C_s close to the detection threshold C_d and decreases considerably for higher concentrations (figure 8). The formation of more and more divided and elongated structures is clearly demonstrated by the evolution of the surface to volume ratio $R = S/V$ (figure 9) which exhibits a continuous increase with time, at a rate that increases as the threshold gets higher.

For a given concentration threshold C_s/C_0 , the S , V and R dependences of the different injection diameters d collapse on a single curve when time is rescaled according to the transformation of equation (3), that is ut/d (figure 9b). This is a direct indication, to which we return in §5, that the fine-scale kinetics of the mixing process involves, like the dispersion properties of the plume discussed in the previous

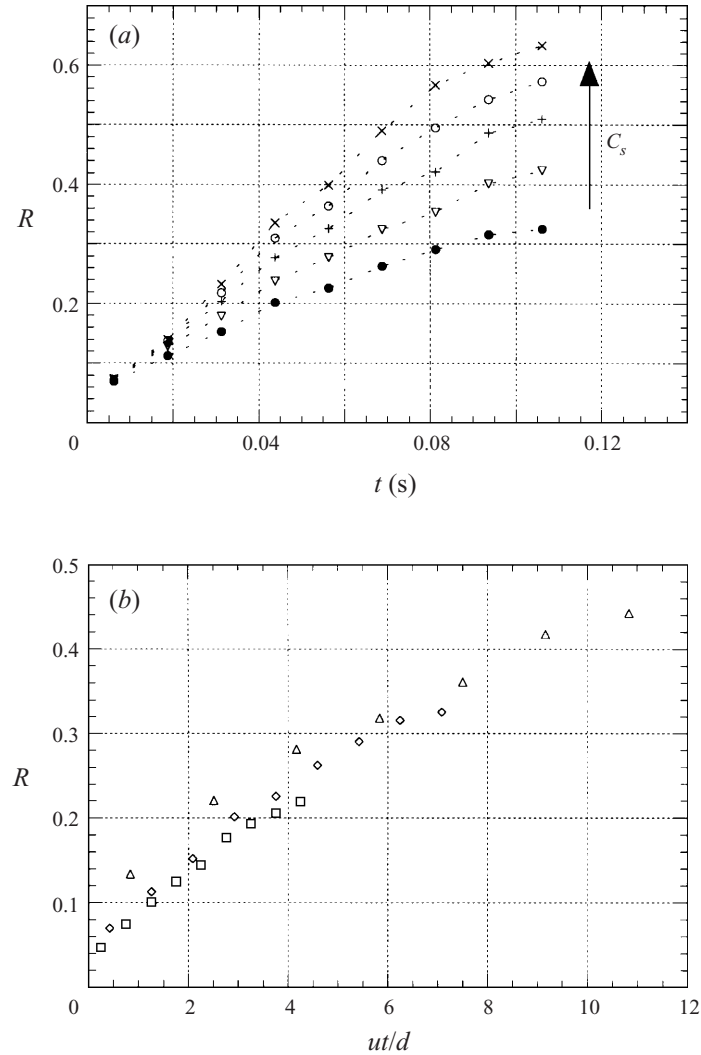


FIGURE 9. (a) Surface to volume ratio as a function of time for different values of threshold height. In the direction of the arrow, $C_s/C_0 = 0.16, 0.25, 0.38, 0.51$ and 0.63 . $d = 0.6$ cm. (b) Surface to volume ratio for $C_s/C_0 = 0.16$ for the three injection sizes \square , $d = 1$ cm; \diamond , $d = 0.6$ cm; \triangle , $d = 0.3$ cm as a function of ut/d .

section, large-scale motions in the flow, or at least motions associated with the injection scale of the dye being mixed.

The scalar volume V is such that the dependences $V_{C_s}(t)$ (volume computed at a given concentration threshold as a function of time, figure 8) and $V_t(C_s)$ (volume computed at a given instant of time as a function of the threshold height, figure 10) both exhibit a similar behaviour, close to an exponential decay. This suggests that the effect of increasing time at constant threshold results in a change of the scalar distribution geometry similar to the change observed by increasing the threshold at constant time.

This equivalence between time and threshold height is very strong. Plotting all the measurements of the volume $V(t, d, C_s)$ obtained for all injection sizes d , times t and

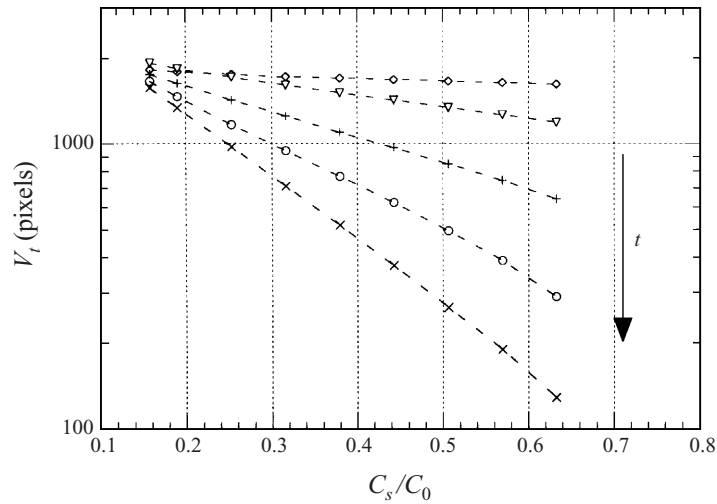


FIGURE 10. Volume of the plume as a function of the threshold height C_s/C_0 for successive instants of time. In the direction of the arrow, $t = 0.006, 0.031, 0.056, 0.081$ and 0.106 s. $d = 0.6$ cm.

thresholds C_s/C_0 , as a function of the dimensionless variable

$$\xi = \frac{ut C_s}{d C_0}, \quad (9)$$

it is seen on figure 11 that all the experimental values collapse on a single curve whose functional form fits the empirical law

$$\frac{V(\xi)}{V_0} = (1 + \xi^\beta) e^{-\alpha\xi}, \quad (10)$$

where $V_0 = w \times d$ is the initial volume occupied by the plume in the first window of width w and $\alpha = 1.02$, $\beta = 1.14$ are the best-fit exponents. Note that the variable ξ incorporates the transformation (3) and expresses, in addition, the relation of the definition of the scalar distribution geometry to the (*a-priori* free) observation threshold.

4.2. Roughness and fractal dimensions

Surface and volume of the scalar distribution are quantities which incorporate contributions of all the scales which contribute to the rugosity, or roughness of the plume. A fractal dimension is an index which measures the relative weight of the different scales in the global roughness. We computed the temporal evolution of the fractal dimension of the two-dimensional objects whose ‘volume’ and ‘surface’ have been defined above for, again, different concentration thresholds.

The procedure is similar to the one described before for the extraction of surfaces and volumes, except that, in order to use a standard box-counting algorithm on two-dimensional images composed of square pixels, we divided each image into square boxes instead of rectangles (other choices can be made, see Catrakis & Dimotakis 1996). The linear size of the computational boxes, w , and their positions on the images have been chosen to cover the plume entirely. The x -coordinate of the centre of each box, x_j , is given by relation (6), for a convection time from the source t_j .

In each box, and for a set of $N = 100$ images, we compute the average number $\bar{N}(r) = (1/N) \sum_{i=1}^N N_i(r)$ of boxes of size r needed to cover the set of non-zero pixels

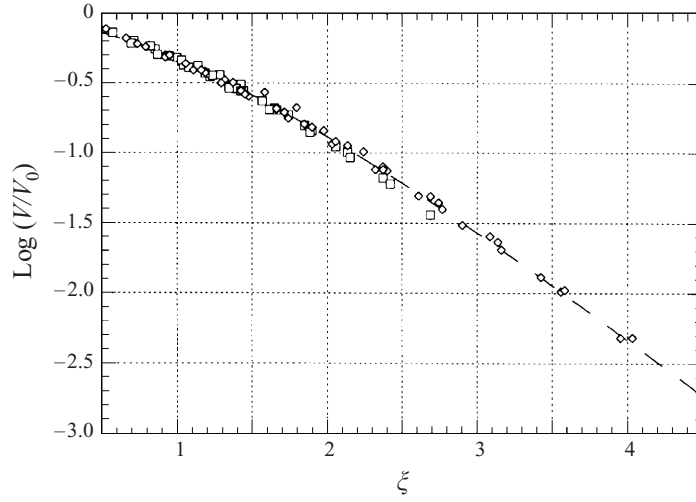


FIGURE 11. Volume of the plume for all diameters of injection, times and concentration thresholds plotted against the similarity variable $\xi = (ut/d)(C_s/C_0)$. The dashed line is the fit of equation (10).

contained in the computational box of image i and located at distance x_j on the image. The procedure is repeated for both the scalar support, or volume, and for its contour, thus providing the fractal dimensions of the object df_o and of its contour df_c , respectively, and for different thresholds C_s as

$$\bar{N}(r) \sim r^{-df}, \quad r = 1, w \text{ pixels.} \quad (11)$$

Since $\bar{N}(r)$ does not follow a pure power law for r for the range of scales covering a whole image and as the apparent dimension is a function of r (see § 5), we define here the exponent df as an average slope in logarithmic coordinates, fitting the $\bar{N}(r)$ versus r dependence in a narrow subrange $\Delta = \{r_{\min} - r_{\max}\}$ with $r_{\min} = 2$ pixels and $r_{\max} = 10$ pixels. This allows the evolution of a single number, df , to be followed as a function of time and concentration threshold, the natural dependence of df on r being discussed separately (§ 5).

We have checked that this procedure is experimentally equivalent to computing the fractal dimension on each image, and then averaging the fractal dimensions. Specifically,

$$df = \frac{1}{N} \sum_{i=1}^N df_i \text{ where } df_i = \left\langle \frac{d \ln N_i(r)}{d \ln r} \right\rangle_{\Delta}$$

was found to be numerically very close to

$$df = \left\langle \frac{d \ln \bar{N}(r)}{d \ln r} \right\rangle_{\Delta} \text{ where } \bar{N}(r) = \frac{1}{N} \sum_{i=1}^N N_i(r).$$

This is consistent with the fact that the distribution of the $N_i(r)$ was found to be peaked around the mean value $\bar{N}(r)$. Correspondingly, the dimension measured on a single image is representative of the mean.

The evolution of df_o and df_c is shown, for $d = 0.6$ cm, as a function of time t and for different thresholds C_s . We chose here $w = 80$ pixels ≈ 1 cm and we partially overlapped consecutive boxes to increase the number of measurement locations in the x -direction. At short times the fractal dimension of the surface (df_c) increases until

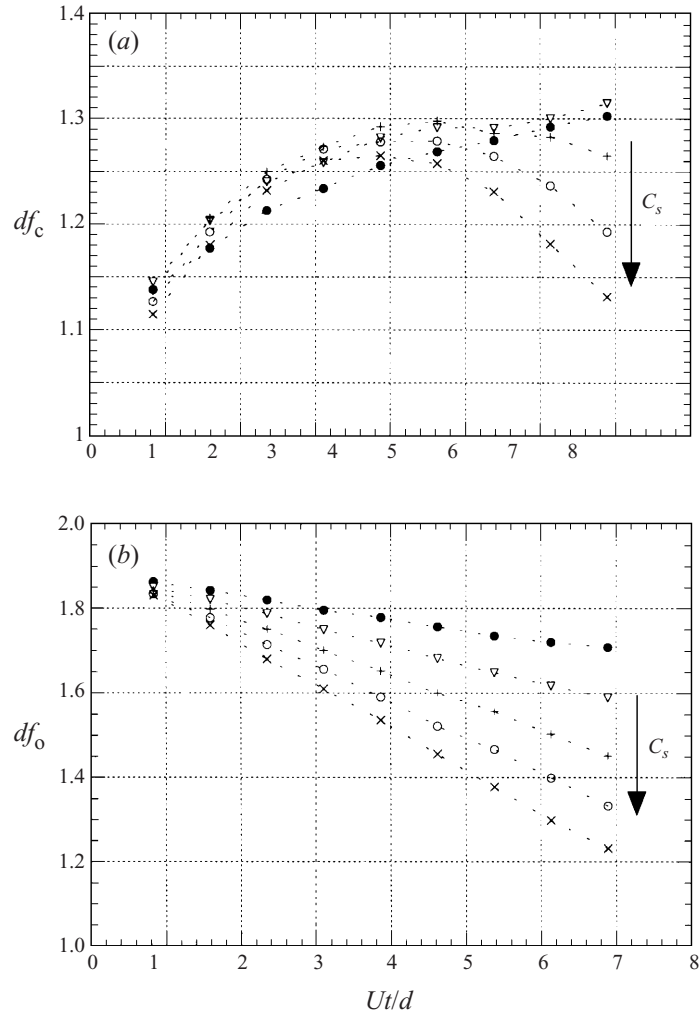


FIGURE 12. Fractal dimensions of the object (*b*) and of its contour (*a*) for different thresholds C_s . In the direction of the arrow, $C_s/C_0 = 0.16, 0.25, 0.38, 0.51$ and 0.63 . $d = 0.6$ cm.

$t \simeq 4d/u$, reaching its maximum value ($\simeq 1.3$). Note that this value is an average, and that maximal dimensions larger than 1.3 are encountered on instantaneous fields, up to 1.4–1.5 typically. Discussing the absolute values of df (Constantin *et al.* 1991; Procaccia & Constantin 1993; Constantin & Procaccia 1994; Cardoso *et al.* 1996), S or V is, as we stress in this paper, of little interest. These are, in essence, variable quantities, and understanding their temporal evolution and dependences on the external parameters ruling the process of mixing seems more useful.

If df_c is fairly threshold independent during its phase of increase in time (figure 12), it becomes strongly dependent on C_s after having reached its maximum, in the decreasing phase. The fractal dimension of the volume df_o is always threshold dependent and decreases regularly towards 1, reflecting the fact that the plume, initially a thick compact object, is progressively converted into a set of elongated sheets. This trend is consistent with the observation that the values of the fractal dimensions of the volume and of the surface tend to approach each other as time

goes on, and this all the more rapidly when the threshold is higher. The structures tend to identify themselves with their boundary.

5. Analysis

5.1. Stirring as a kinematic construction

It is known that the deformation tensor in turbulent flows has, in the mean, two directions of stretching and one direction of compression (Betchov 1956) and that this property leads to the increase of the length and area of material lines and surfaces (Batchelor & Townsend 1956). The condition for the net increase of lengths and area was later recognized to be even weaker, and such that only incompressibility and isotropy of the flow is required (Cocke 1969; Orszag 1970). In a multiscale flow, i.e. in a flow where the velocity difference (we mix here Lagrangian and Eulerian estimates) $\delta u(r)$ separated by a distance r is a function of r as $\delta u(r) \sim u(r/d)^\zeta$, Villermaux & Gagne (1994) showed that, provided the r -dependence of $\delta u(r)$ is convex (i.e. $\zeta < 1$), the increase of the length of a material line in time is itself scaled dependent, and that small scales contribute more to the net increase than larger ones. From this the fractality of material lines and surfaces originates, explaining how an initially straight and smooth contour gets more and more corrugated as time elapses.

Let us summarize the main idea. Consider an initially smooth scalar blob of linear size d . The number of boxes needed to cover its contour $N(r, 0)$ is of order d/r , in two dimensions ($(d/r)^2$ in three dimensions). We assume that the blob has been formed in a flow field with prescribed stationary velocity increments $\delta u(r)$ like in the present experiments. Now, after a time t not too large compared to $t(r) = r/\delta u(r)$, the number of segments needed to cover the contour is

$$N(r, t) = N(r, 0) \left[1 + \frac{t}{t(r)} \right]. \quad (12)$$

The origin of the fractality is clear from this: provided $t(r) \sim (d/u)(r/d)^{1-\zeta}$ is an increasing function of r , that is provided $\zeta < 1$, the corrective factor to the trivial factor $N(r, 0) = d/r$ in $N(r, t)$ of equation (12) increases as the scale r decreases. Recasting (12) in the form of a power law (although one sees that the dynamics does not generate pure power laws) $N(r, t) \sim N_0(r/d)^{d_c(r,t)}$, it is clear that both a scale r and a time t dependence of the local, apparent fractal dimension $d_c(r, t)$ can be expected.

This is a purely kinematic argument. Note that, as it stands, it accounts for the roughly linear temporal increase of what we called the surface of the blob, that is the length of its contour measured at the resolution scale r_{\min} and which is proportional to $N(r_{\min}, t)$ (figure 7). But the purely geometrical argument of equation (12) does not incorporate the fact that the ‘line’ defining the contour of the blob eventually fades away and disappears by diffusive spreading.

5.2. The blurring action of diffusion

At a given instant of time, the extent and structure of a diffuse interface is the result of two opposing, continuous processes: the birth of new structures at a rate prescribed, according to (12), by their size through the characteristic time $t(r)$, and the destruction of these structures due to their dilution in the medium by molecular diffusion. We investigate now the interplay between these two effects to give a realistic model of the flow field in connection with the experiments reported here and we purposely confine our analysis to the case of a line. The extension of the analysis to a surface (a scalar blob immersed in the three-dimensional space), as for mixing in the real

world, is straightforward. The reasoning is not sensitive to the precise form of the field of velocity increments $\delta u(r)$ provided that (i) it exhibits a convex shape on r and that (ii) it has a regular functional dependence $\delta u(r) \sim r/d$ in the small r -limit (see Villermaux & Gagne 1994).

We model the field of velocity increments in the following manner: the maximal mean velocity difference which can be encountered in the flow equals the mean velocity of the carrier flow itself, that is u , and is likely to be encountered at large separation distances r . At smaller scales, due to the regularizing action of the viscosity in the dissipative range, only simple shear or solid rotation is allowed so that $\delta u(r) \sim r$. We choose the crossover lengthscale as the size of the blob d , thus expressing that the motions which appreciably distort the blob are those associated with scales of the order of its own size. Thus $\delta u(r)$ has the form

$$\frac{\delta u(r)}{u} = f\left(\frac{r}{d}\right) \quad (13a)$$

with

$$f\left(\frac{r}{d}\right) = \frac{r/d}{1+r/d}, \quad (13b)$$

the crossover function $f(r/d)$ being chosen here in the form of a Batchelor-like parametrization (Batchelor 1951, see also Durbin 1980, Sawford & Hunt 1986) for analytical convenience, with d as the crossover scale. Provided the two above limits (i) and (ii) are fulfilled, the precise mathematical shape of $f(r/d)$ is not crucial for the present discussion and other forms would lead to the same conclusions.

Stretching on the contour of a fluid element is, as expressed by (12), at the root of its corrugation process. Cumulated stretching with variable persistency also explains, as shown by Villermaux *et al.* (1998), the existence of a wide distribution of concentration levels. The PDF of concentration resulting from the transient mixing of a scalar blob of initial size d is given, in the present set-up, by

$$P\left(\frac{C}{C_0}\right) \sim \exp\left(-\frac{t}{t_s} \frac{C}{C_0}\right) \quad \text{for } t \gg t_s, \quad (14)$$

a time t after the release of the blob in the medium, with

$$t_s = 0.12 \frac{d}{u} \ln(5Sc) \quad (15)$$

being the mixing time, proportional to the injection timescale d/u in the medium. Thus, the fraction of fluid elements constituting the blob whose concentration is larger than a given concentration threshold C_s (with $0 < C_s < C_0$) is

$$\int_{C_s}^{C_0} P\left(\frac{C}{C_0}\right) dC \sim \exp\left(-\frac{t}{t_s} \frac{C_s}{C_0}\right) \quad (16)$$

to leading order. This fraction of elements having ‘survived’ has a direct geometrical interpretation. What we called the volume of the blob $V(\xi)$, with $\xi = (ut/d)(C_s/C_0)$ is given by the number of fluid elements whose concentration is larger than C_s at time t , and we have found (equation (10)) that $V(\xi) \sim V(0) \exp(-\alpha\xi)$ with $\alpha = 1.02$, for large ξ . This result is nicely consistent with (15) and (16) since

$$\frac{t}{t_s} \frac{C_s}{C_0} = \frac{ut}{0.12d \ln 5Sc} \frac{C_s}{C_0} \approx 0.9 \frac{ut}{d} \frac{C_s}{C_0}$$

with $Sc = 2000$, the prefactor 0.9 being essentially very close to $\alpha = 1.02$.

The relation (12), giving the number of segments covering the contour of the blob, is thus modified to account for the destruction by diffusion as

$$N(r, t, C_s) = N(r, 0) \left[1 + \frac{t}{t(r)} \exp\left(-\frac{t}{t_s} \frac{C_s}{C_0}\right) \right] \quad (17)$$

with $t(r) = r/\delta u(r)$ and $\delta u(r)$ being given by (13a) and (13b). For a fixed scale r and concentration threshold C_s , the number $N(r, t, C_s)$ first increases linearly with time and independently of the threshold C_s because of the production term $t/t(r)$. Then $N(r, t, C_s)$ decreases by the exponential damping factor because the concentration of all the fluid elements being continuously stretched progressively falls below C_s , this last process ‘erasing’ the action of the first one. This trend reflects the evolutions of the blob surfaces reported on figure 7.

The relative contribution of the different scales r to the increase of the blob surface is measured by the fractal dimension of the contour defined by $N(r, t, C_s) \sim N_0(r/d)^{d_c(r, t, C_s)}$. As noted above, since neither (12) nor (13) exhibit pure power laws in r , we expect $d_c(r, t, C_s)$ to be both a function of time and scale, but also a function of the threshold C_s/C_0 defining the contour. Together with (12), (13) and noting that $N(r, 0) \sim d/r$, (17) is written as

$$N(r, t, C_s) \sim \frac{1}{z} \left[1 + \frac{B}{1+z} \right] \quad (18a)$$

with

$$B = \frac{ut}{d} \exp\left(-\frac{t}{t_s} \frac{C_s}{C_0}\right) \quad (18b)$$

and

$$z = \frac{r}{d}. \quad (18c)$$

Elementary manipulations show that the dimension $d_c(r, t, C_s) = -d \ln N / d \ln r$ is

$$d_c(r, t, C_s) = 1 + \frac{Bz}{(1+z)^2 + B(1+z)} \xrightarrow{z \rightarrow 0} 1 + \frac{B}{1+B}z \quad (19)$$

that is, for $r/d \ll 1$ and $t \gg t_s$,

$$d_c(r, t, C_s) \approx 1 + \frac{ut}{d} \exp\left(-\frac{t}{t_s} \frac{C_s}{C_0}\right) \frac{r}{d}. \quad (20)$$

For a given concentration threshold C_s and time t , the ‘dimension’ $d_c(r, t, C_s)$ is an increasing function of the scale r . This last point has been demonstrated and studied in great details by Catrakis & Dimotakis (1996) who showed that the fractal dimension of the cross-section contour of a turbulent jet measured in a fixed frame goes gradually from 1 (smooth frontier at the small scales) to 2 (space-filling object at large scales). Catrakis & Dimotakis designated these objects as *scale-dependent fractals* and they also noted the weak dependence of the $N(r, C_s)$ versus r relationship on the Reynolds number (measurable, however), as well as the Reynolds number independence of the large excursion wing of the concentration PDF, consistently with (14) and (15). This Reynolds number independence goes back, in fact, to the Reynolds number independence of the mixing time in turbulent flows (see e.g. Nagata 1975, equation (15) and Villermaux *et al.* 1998).

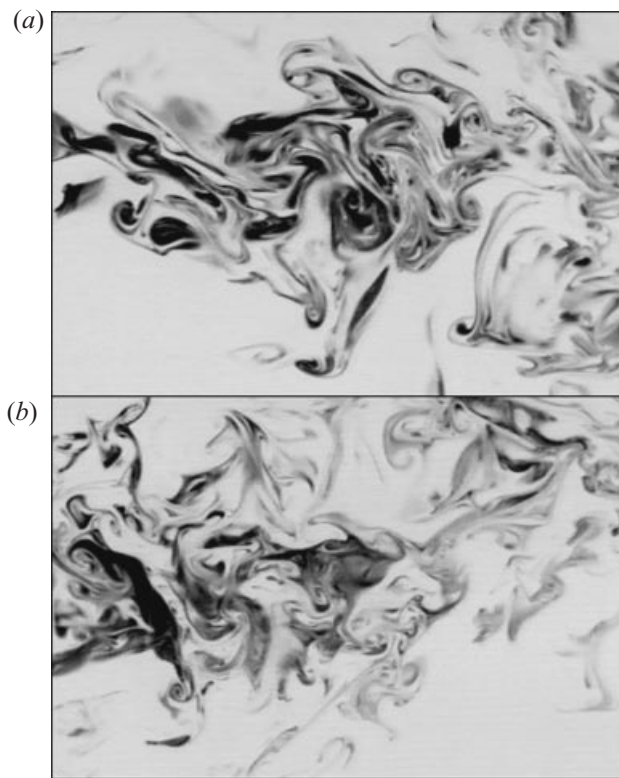


FIGURE 13. Instantaneous images of the scalar distribution recorded for distances $8 < x/d < 12$ downstream of the injection point, with $d = 1$ cm for two different carrier fluid velocities corresponding to (a) $Re = u'L/\nu = 6000$ and (b) $Re = 12000$.

The fact that the $N(r, C_s)$ versus r dependence is continuously bent is due to the iterative construction of the contour (equation (12)) and to the convex r -dependence of the field of velocity increments $\delta u(r)$, going gradually from a regular behaviour $\delta u(r) \sim r$ to a turbulent one $\delta u(r) \sim r^\zeta$ (with $\zeta = 0$ in the present analysis, see equations (13a) and (13b)) through the crossover function $f(r/d)$.

As an illustration, consider the pictures of figure 13. They represent instantaneous images of the scalar field for distances such that $8 < x/d < 12$ downstream of the injection point, with $d = 1$ cm for two different carrier fluid velocities corresponding to $Re = 6000$ and $Re = 12000$, respectively. The concentration PDFs of these two images (figure 14) are superimposable (within the fluctuations due to the limited statistical convergence on a single image) suggesting a Reynolds number independence of the mixture structure consistently with (14) and (15). They exhibit an exponential tail with an argument close to 6 corresponding to that distance and to $Sc = 2000$ (Villermaux *et al.* 1998). The iso-concentration contours of figure 13 are shown on figure 15 for four different concentration thresholds $C_s/C_0 = 0.2, 0.3, 0.4$ and 0.5 . These values are chosen to be clearly in the exponential part of the PDF, and within sufficiently converged probability levels.

Obviously, the regions of the flow with a concentration level above a given threshold C_s are less and less numerous, more and more sparse as C_s is increased, consistently with the decaying shape of the PDF. The pictures of figure 15 all correspond to the same instant of time, and they only differ by an increased threshold. The same trend

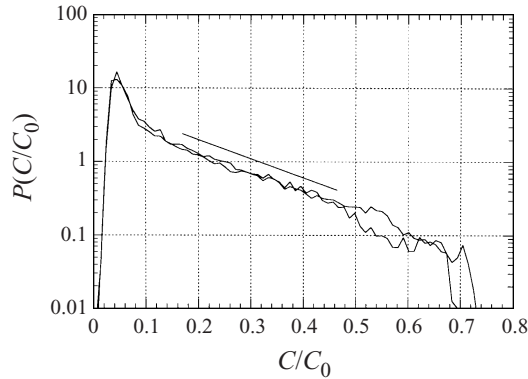


FIGURE 14. Concentration PDFs of the scalar fields of the pictures shown on figures 13(a) and 13(b). Within the fluctuations due to the limited statistical convergence on a single image, the two PDF's are superimposable and exhibit an exponential decrease whose argument is close to 6 (straight line).

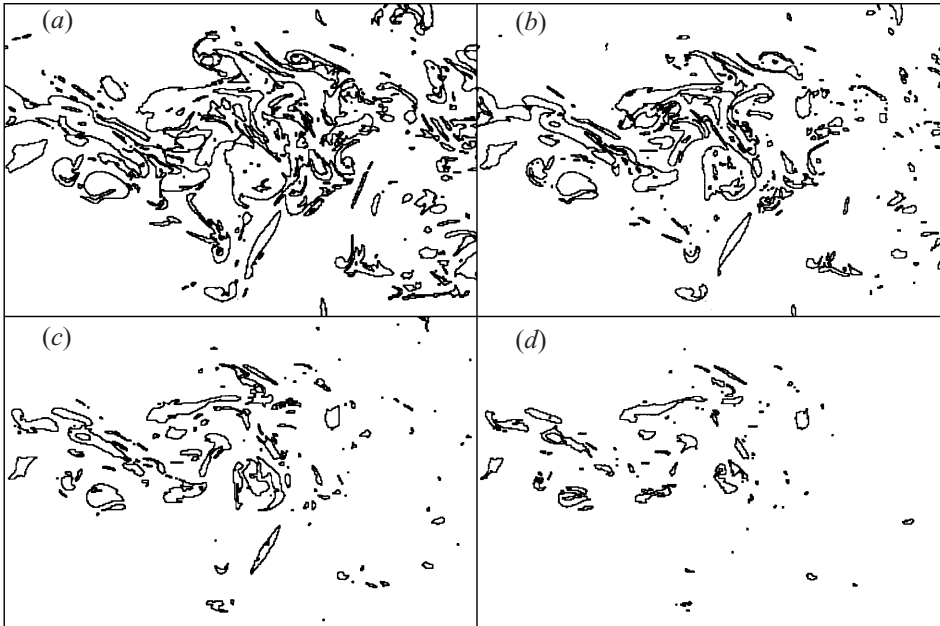


FIGURE 15. Contours of the level sets of the scalar field of figure 13(a), for four different concentration thresholds heights. (a) $C_s/C_0 = 0.2$, (b) 0.3, (c) 0.4 and (d) 0.5.

would be observed for a given C_s , and increasing time t (see figures 2, 6 and §4.1). The equivalence of the roles played by time t and C_s on the morphology of a blob of scalar being mixed is expressed by the fact that the argument of the concentration PDF involves the product of C_s and t , as emphasized in §4.1, and by equations (14) and (17).

Figure 16 shows the number of boxes $N(r, C_s)$ needed to cover the different iso-concentration contours obtained by a standard box-counting algorithm for the four values of C_s/C_0 , fitted by relation (18), B being the fitting parameter. The fit is reasonably good, although not perfect, and accounts for the continuous curvature of the $N(r, C_s)$ versus r dependence with a local slope going from -1 to -2 as r increases.

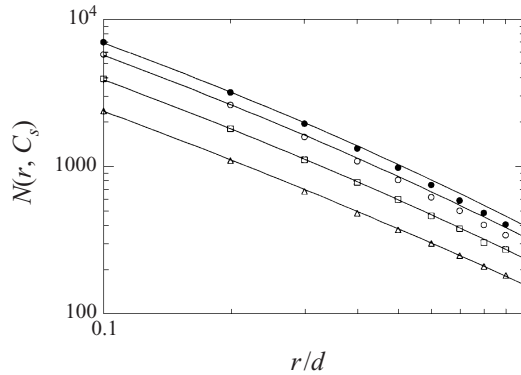


FIGURE 16. Box-counting relationships for the isoconcentration contours of figure 15. $C_s/C_0 = 0.2$ (\bullet), 0.3 (\circ), 0.4 (\square), 0.5 (\triangle). Continuous line: fit by equation (18).

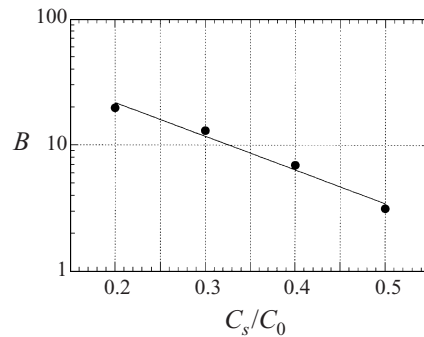


FIGURE 17. Fitting parameter of equation (18) for the threshold levels of figures 15 and 16.

The parameter B is expected to follow an exponential decrease with C_s/C_0 , with an argument identical to that of the global concentration PDF (see (14) and (17)). This is not contradictory to figure 17 where the best-fit value of B is plotted against each value of C_s/C_0 . The constant B is found to decay exponentially with C_s/C_0 , with an argument close to 6, identical to that of the concentration PDF (figure 14).

The curvature of $N(r, C_s)$ becomes more pronounced as C_s/C_0 gets lower. This trend, already noticeable on the data of Sakai *et al.* (1995) is due to the fact that the correction to the pure and trivial power-law dependence (r^{-1}) is weighted by B , a constant which decreases with C_s/C_0 (equation (18)).

5.3. Average dimensions on a narrow spatial interval

The functional dependence of $N(r, C_s, t)$ on r curves continuously from r^{-1} at small scales (respectively r^{-2} in three dimensions) to a steeper dependence at larger scales for times t larger than the mixing time t_s . This feature is due to the iterative increasing complexity of contours (equation (12)), and to the regular change of the stirring law, through the function $f(r/d)$ as the scale is varied from small to large. The conjunction of these two factors results in a non-pure-power-law dependence of $N(r, C_s, t)$ on r , implying a fractal dimension $d_c(r, t, C_s)$ which depends on scale.

Nevertheless, it may appear useful, as in the present experiments (see §4.2), to follow the temporal evolution of an average $\bar{d}_c(t, C_s)$ of $d_c(r, t, C_s)$ over a given fixed

range of scales $\Delta = \{r_{\min} - r_{\max}\}$ as

$$\bar{d}_c(t, C_s) = \frac{1}{\ln(r_{\max}/r_{\min})} \int_{r_{\min}}^{r_{\max}} d_c(r, t, C_s) d(\ln r), \quad (21)$$

the average being performed at logarithmic scales. Clearly

$$\bar{d}_c(t, C_s) = \frac{\ln(N(r_{\min}, t)/N(r_{\max}, t))}{\ln(r_{\max}/r_{\min})}.$$

Note that the procedure (21) is implicitly the same as drawing a straight line on a log-log plot of $N(r, C_s, t)$ versus r close to the resolution scale r_{\min} of the iso-concentration contour. Using (20) as an estimate of the behaviour of $d_c(r, t, C_s)$ in the small- r limit, we get

$$\bar{d}_c(t, C_s) \approx 1 + \frac{ut}{d} \exp\left(-\frac{t}{t_s} \frac{C_s}{C_0}\right) \frac{r_{\max}/d}{\ln(r_{\max}/r_{\min})} \quad (22)$$

if the average has been extended up to r_{\max} such that $r_{\min} \ll r_{\max} < d$ as for the present experiments. The average (22) is a weak function of the outer integration limit, and therefore the value of $\bar{d}_c(t, C_s)$ is weakly dependent on the choice of the extent of the averaging region.

The average dimension $\bar{d}_c(t, C_s)$ is a function of time and concentration threshold. The concentration threshold dependence of $\bar{d}_c(t, C_s)$ for fixed t was already noted by Lane-Serff (1993) (although he mentions he did not fully clarify the role of the noise in his results) and by Flohr & Olivari (1994) who found an evolution of the dimension in the cross-section of a jet very similar to ours in figure 12(a): for a given time, the apparent dimension $\bar{d}_c(t, C_s)$ is decreasing as C_s/C_0 is increased, ultimately relaxing towards 1.

It is interesting to note that the high threshold limit of $\bar{d}_c(t, C_s)$ is closer to 1 than to 0, suggesting that the shape of the structures with the strongest concentration in a scalar turbulent field is close to a sheet with homogeneous concentration (whose intercept with the visualization plane is a line with dimension 1) instead of a filament (whose intercept would be a point of dimension 0). The stretched sheet is, as noted long ago (see e.g. Ranz 1979), the paradigm of scalar mixing.

6. Conclusions

Watching the evolution of a scalar plume initially segregated from the surrounding turbulent medium in which it is ultimately diluted has revealed that the process of mixing is a transient process of birth and death of complexity.

Mixing, as suggested by our common sense, is the operation by which a system evolves from one state of simplicity (the initial segregation) to another state of simplicity (complete uniformity). Between these two extremes, complex patterns are born, and die. Two questions then naturally arise: how can the complex pattern geometry be characterized, and what is the clock, the timescale of the process?

The present study has shown that, at least in the case of a scalar deposited by a small tube (smaller than the integral scale of the turbulence, but larger than the dissipative scales) in the sustained turbulent field of a jet, the clock is set by the injection time d/u . This timescale appears both in the mean dispersion properties of the scalar distribution (§3) and in the fine-scale evolution laws of the mixture (§4). The fact that the kinetics of the uniformization process involves large-scale features of the flow and of the initial scalar distribution only, thus curiously bypassing the hierarchical

structure of turbulence, reflects the well-known Reynolds number independence of mixing times (Nagata 1975; Villermaux *et al.* 1998).

The intimate structure of the mixture consists of stretched sheets whose transverse size gets thinner and thinner as time progresses (see e.g. the surface to volume ratio on figure 9), and then they fade away by the smoothing action of molecular diffusion (figures 7 and 8).

In the course of time, two concomitant, opposing processes occur: a process of birth of new structures by the underlying motions, dominant at short times, and then a process of uniformization, dominant in the last stages. The crossover time depends on the concentration threshold of observation (see figures 7 and 12). At a given instant of time, the mixture does not exhibit the same shapes; it has not the same geometrical structure when the level of concentration threshold is varied. The relation of the scalar field geometry to the concentration level height chosen to define it is expressed by the rescaling variable $\xi = (ut/d)(C_s/C_0)$, omnipresent in the experimental evidence (figures 11 and 12), and in the analysis (§5).

The interplay between these two effects is best illustrated by equation (17) giving, in our analysis, the number of boxes of size r needed to cover the contour of a scalar blob:

$$N(r, t, C_s) = N(r, 0) \left[1 + \frac{t}{t(r)} \exp\left(-\frac{t}{t_s} \frac{C_s}{C_0}\right) \right].$$

This relation illustrates the effect of the competition between the production factor $t/t(r)$ and the dissipation $\exp(-t/t_s)(C_s/C_0)$ on the total extent of the blob interface, and also on its hierarchical (fractal) structure.

In the same manner as all the geometrical features of the scalar distribution were found to depend on time t and concentration threshold C_s/C_0 , fractal dimensions were found to depend in addition on scale, showing that if the geometry is related to time and level of observation, it is also related to the spatial scale of observation and is a non-scale-invariant quantity (figures 12 and 16).

The nature of mixing is transient, and the laws which describe it express crossovers between trivial extremes. The very essence of the process has not been better expressed than by Henri Bergson in *L'évolution créatrice* (1941): 'Ce qui est réel, c'est le changement continu de forme: *la forme n'est qu'un instantané pris sur une transition.*', which could be translated by: 'What is real is the ceaseless change of shape: *the shape is nothing but a snapshot taken on a transition.*'

REFERENCES

- ANTONIA, R. A., SATYAPRAKASH, B. R. & HUSSAIN, A. K. M. F. 1980 Measurements of dissipation rate and some other characteristics of turbulent plane and circular jets. *Phys. Fluids* **23**, 695–699.
- BATCHELOR, G. K. 1951 Pressure fluctuations in isotropic turbulence. *Proc. Camb. Phil. Soc.* **47**, 359–374.
- BATCHELOR, G. K. 1959 Small-scale variation of convected quantities like temperature in a turbulent fluid. Part 1. General discussion and the case of small conductivity. *J. Fluid Mech.* **5**, 113–133.
- BATCHELOR, G. K., HOWELLS, I. D. & TOWNSEND, A. A. 1959 Small-scale variation of convected quantities like temperature in a turbulent fluid. Part 2. The case of large conductivity. *J. Fluid Mech.* **5**, 134–139.
- BATCHELOR, G. K. & TOWNSEND, A. A. 1956 Turbulent diffusion. In *Surveys in Mechanics* (ed. G. K. Batchelor & R. M. Davis), pp. 352–399. Cambridge University Press.
- BETCHOV, R. 1956 An inequality concerning the production of vorticity in isotropic turbulence. *J. Fluid Mech.* **1**, 497–504.

- BERGSON, H. 1941 *L'évolution Créatrice*. Presses Universitaires de France, Paris.
- BREIDENTHAL, R. 1981 Structure in turbulent mixing layers and wakes using a chemical reaction. *J. Fluid Mech.* **109**, 1–24.
- BROWN, G. L. & ROSHKO, A. 1974 On density effects and large structure in turbulent mixing layers. *J. Fluid Mech.* **64**, 775–816.
- CARDOSO, O., GLUCKMAN, B., PARCOLLET, O. & TABELING, P. 1996 Dispersion in quasi-two-dimensional turbulent flow: An experimental study. *Phys. Fluids* **8**, 209–214.
- CATRAKIS, H. J. & DIMOTAKIS, P. E. 1996 Mixing in turbulent jets: scalar measures and isosurface geometry. *J. Fluid Mech.* **317**, 369–406.
- COCKE, W. J. 1969 Turbulent hydrodynamic stretching: Consequences of isotropy. *Phys. Fluids* **12**, 2488–2492.
- CONSTANTIN, P. & PROCACCIA, I. 1994 The geometry of turbulent advection: sharp estimates for the dimension of the level sets. *Nonlinearity* **7**, 1045–1054.
- CONSTANTIN, P., PROCACCIA, I. & SREENIVASAN, K. R. 1991 Fractal geometry of isoscalar surfaces in turbulence: theory and experiments. *Phys. Rev. Lett.* **67**, 1739–1742.
- CORRSIN, S. 1951 On the spectrum of isotropic temperature fluctuations in an isotropic turbulence. *J. Appl. Phys.* **22**, 469–473.
- CORRSIN, S. 1964 The isotropic turbulent mixer: Part II. Arbitrary Schmidt number. *AIChE J.* **10**, 870–877.
- CSANADY, G. T. 1973 *Turbulent Diffusion in the Environment*. D. Reidel.
- DAMKÖHLER, D. 1940 Der Einfluss der Turbulenz auf die Flammengeschwindigkeit in Gasgemischen. *Z. Elektroch.* **46**, 601–652.
- DANCKWERTS, P. V. 1953 Continuous flow systems. Distribution of residence times. *Chem. Engng Sci.* **2**, 1–15.
- DURBIN, P. A. 1980 A stochastic model for two particle dispersion and concentration fluctuations in homogeneous turbulence. *J. Fluid Mech.* **100**, 279–302.
- FLOHR, P. & OLIVARI, D. 1994 Fractal and multifractal characteristics of a passive scalar dispersed in a turbulent jet. *Physica D* **76**, 278–290.
- FREDERIKSEN, R. D., DAHM, J. A. & DOWLING, D. R. 1996 Experimental assessment of fractal scale-similarity in turbulent flows. Part I. One-dimensional intersections. *J. Fluid Mech.* **327**, 35–72.
- GLUCKMAN, B. J., WILLAIME, H. & GOLLUB, J. P. 1993 Geometry of isothermal and isoconcentration surfaces in thermal turbulence. *Phys. Fluids A* **5**, 647–661.
- HAWTHORNE, W. R., WENDELL D. S. & HOTTEL, H. C. 1949 Mixing and combustion in turbulent gas jets. In *Third Symp. on Combustion and Flame and Explosion Phenomena, Baltimore*, pp. 266–288. Williams & Wilkins.
- HUANG, L.-S. & HO, C.-M. 1990 Small-scale transition in a plane mixing layer. *J. Fluid Mech.* **210**, 475–500.
- KARASSO, P. S. & MUNGAL, M. G. 1996 Scalar mixing and reaction in plane liquid shear layers. *J. Fluid Mech.* **323**, 23–63.
- KOOCHESFAHANI, M. M. & DIMOTAKIS, P. E. 1986 Mixing and chemical reaction in a turbulent liquid mixing layers. *J. Fluid Mech.* **170**, 83–112.
- LANE-SERFF, G. F. 1993 Investigation of the fractal structure of jets and plumes. *J. Fluid Mech.* **249**, 521–534.
- MANDELBROT, B. B. 1975 On the geometry of homogeneous turbulence, with stress on the fractal dimension of the iso-surfaces of scalars. *J. Fluid Mech.* **72**, 401–416.
- MENEVEAU, C. & SREENIVASAN, K. R. 1990 Interface dimension in intermittent turbulence. *Phys. Rev. A* **41**, 2246–2248.
- MILLER, P. L. & DIMOTAKIS, P. E. 1991 Stochastic geometric properties of scalar interfaces in turbulent jets. *Phys. Fluids A* **3**, 168–177.
- NAGATA, S. 1975 *Mixing, Principles and Applications*. John Wiley & Sons.
- NICOLLEAU, F. 1996 Numerical determination of turbulent fractal dimensions. *Phys. Fluids* **8**, 2661–2670.
- OBOUKHOV, A. M. 1949 Structure of the temperature field in a turbulent flow. *Izv. Acad. Nauk SSSR, Geogr. Geofiz* **13**, 58–69.
- ORSZAG, S. A. 1970 Comments on 'Turbulent hydrodynamic line stretching: Consequences of isotropy'. *Phys. Fluids* **12**, 2203–2204.

- OTTINO, J. M. 1989 *The Kinematics of Mixing: Stretching, Chaos, and Transport*. Cambridge University Press.
- PRASAD, R. R. & SREENIVASAN, K. R. 1990 The measurement and interpretation of fractal dimensions of the scalar interface in turbulent flows. *Phys. Fluids A* **2**, 792–807.
- PROCACCIA, I. & CONSTANTIN, P. 1993 The fractal geometry of the level sets of a contaminant dispersed by chaotic waves. *Europhys. Lett.* **22**, 689–694.
- RAMSHANKAR, R. & GOLLUB, J. P. 1991 Transport by capillary waves. Part II: Scalar dispersion and structure of the concentration field. *Phys. Fluids A* **3**, 1344–1350.
- RANZ, W. E. 1979 Application of a stretch model to mixing, diffusion and reaction in laminar and turbulent flows. *AIChE J.* **25**, 41–47.
- REYNOLDS, O. 1894 Study of fluid motion by means of coloured bands. *Nature* **50**, 161–164.
- RICHARDSON, L. F. 1926 Atmospheric Diffusion shown on a distance-neighbour graph. *Proc. R. Soc. Lond. A* **110**, 709–737.
- SAKAI, Y., NAKAMURA, I., LIU, S. & NAKATA, K. 1995 On fractal features of diffusion field in a turbulent jet. In *Advances in Turbulence V* (ed. R. Benzi), pp. 445–449. Kluwer.
- SAWFORD, B. L. & HUNT J. C. R. 1986 Effects of turbulence structure, molecular diffusion and source size on scalar fluctuations in homogeneous turbulence. *J. Fluid Mech.* **165**, 373–400.
- SREENIVASAN, K. R., RAMSHANKAR, R. & MENEVEAU, C. 1989 Mixing, entrainment and fractal dimensions of surfaces in turbulent flows. *Proc. R. Soc. Lond. A* **421**, 79–108.
- STAPOUNTZIS, H., SAWFORD, B. L., HUNT J. C. R. & BRITTER, R. E. 1986 Structure of the temperature field downwind of a line source in grid turbulence. *J. Fluid Mech.* **165**, 401–424.
- TAYLOR, G. I. 1921 Diffusion by continuous movements. *Proc. Lond. Math. Soc.* **20**, 196–212.
- TAYLOR, G. I. 1953 Dispersion of a soluble matter in a solvent flowing slowly through a tube. *Proc. R. Soc. Lond. A* **218**, 44–59.
- TONG, C. & WARHAFT, Z. 1995 Passive scalar dispersion and mixing in a turbulent jet. *J. Fluid Mech.* **292**, 1–38.
- VILLERMAUX, E. 1995 Fast bimolecular reactions in homogeneous turbulence: Structure of the reactive interface and surface of reaction. In *Advances in Turbulence V* (ed. R. Benzi), pp. 529–533. Kluwer.
- VILLERMAUX, E. & GAGNE, Y. 1994 Line dispersion in homogeneous turbulence: stretching, fractal dimensions and micromixing. *Phys. Rev. Lett.* **73**, 252–255.
- VILLERMAUX, E., INNOCENTI, C. & DUPLAT, J. 1998 Scalar fluctuations PDF's in transient turbulent mixing. *C. R. Acad. Sci. Paris* **326** (Série IIb), 21–26.
- WELANDER, P. 1955 Studies on the general development of motion in a two-dimensional, ideal fluid. *Tellus* **7**, 141–156.